Nanoscale Advances

ROYAL SOCIETY OF CHEMISTRY

PAPER

View Article Online
View Journal | View Issue

Cite this: *Nanoscale Adv.*, 2020, **2**, 4062

UV–O_3 treated annealing-free cerium oxide as electron transport layers in flexible planar perovskite solar cells†

Aiying Pang,[ab] Jinlong Li,[ac] Xiao-Feng Wei,[d] Zhi-Wu Ruan,[ab] Ming Yang[ab] and Zhong-Ning Chen *[ab]

Fabricating electron transport layers at low temperatures is challenging but highly desired in the field of flexible perovskite solar cells (f-PSCs). In this study, highly uniform cerium oxide (CeO_x) films prepared by the UV–O_3 treatment have been successfully applied as the electron transport layer (ETL) in methylammonium lead halide ($CH_3NH_3PbI_3$) perovskite-based f-PSCs. Under AM 1.5 G sunlight with 100 mW cm^{-2}, these cells exhibited an open-circuit voltage (V_{oc}) of 0.98 V, a short-circuit current density (J_{sc}) of 19.42 mA cm^{-2}, a fill factor (FF) of 0.72 and power conversion efficiency (PCE) of 14.63%. The PCE was much higher than that of the control planar CeO_x ETL (PCE ~ 9.08%) prepared at a low temperature (80 °C) without the UV–O_3 treatment, and this was ascribed to the improved CeO_x film, enhanced light absorption and suppressed charge recombination. The cells that bend at 15 mm of radius showed excellent stability with less than 10% reduction in PCE after 500 cycles of repeated bending at ambient temperature. The charge-transmission kinetic parameters and long-term stability of the CeO_x-based f-PSCs were analyzed as well.

Received 6th May 2020
Accepted 14th July 2020

DOI: 10.1039/d0na00367k

rsc.li/nanoscale-advances

1. Introduction

Perovskite solar cells (PSCs) are very promising devices in photovoltaic applications due to their impressive efficiency increasing and efficient energy harvesting. Most academic and industrial researches have been focused on PSCs immobilized on rigid substrates.[1,2] However, rigid glass substrates are generally fragile and difficult for scale-up utilization. Incontrovertibly, the flexible perovskite solar cells (f-PSCs) hinged on plastic substrates, which are readily bendable and expediently portable, are suitable for wearable electricity-generating devices and building integrated photovoltaics. In fact, relevant advancements in n–i–p planar or p–i–n cells on plastic substrates achieved the highest reported power conversion efficiency (PCE) of 20.01%.[3–5] Apart from the high PCE, this new photovoltaic technology can be achieved using low temperatures (<150 °C) to convert the perovskite and electron transport layer (ETL) precursors into their final semiconducting forms, which are then immobilized onto transparent plastic substrates, such as polyethylene naphthalate (PEN) and polyethylene terephthalate (PET).

Nevertheless, some new obstacles have been found in f-PSCs. Titanium oxide (TiO_2), the most widely used material in the compact layer and mesoporous layer (collectively called ETL) in the regular architecture of PSCs, typically sustains high-temperature treatment (500 °C).[6,7] This is incompatible with plastic substrates, whose processing temperature must be controlled below 150 °C. Till now, only one study has reported the use of mesoporous TiO_2 in f-PSCs made of polymer films,[8] whereas it is more regularly used on metal-foil substrates that can endure high temperatures.[9] In addition, Nb-doped TiO_2 ETLs fabricated *via* a low-temperature (<50 °C) UV process exhibited the best PCE of 16.01% when used in n–i–p f-PSCs.[10] ETLs generated from Ti-based metal–organic framework nanoparticles at ambient temperature have been found suitable for charge injection and transfer from the perovskite to the electrodes.[11] Although a TiO_x-based ETL prepared through a low-temperature (<100 °C) solution process has achieved up to 17.6% of PCE, TiO_2-based PSCs can be easily destroyed by UV light.[12] This intrinsic property inhibits the commercial applications of TiO_2-based PSCs.[13,14] ZnO is considered as the most promising material for f-PSCs because it has the same conduction band at 3.2 eV as that of TiO_2, a higher electron mobility of 115–155 $cm^2\ V^{-1}\ s^{-1}$ and especially an easier low-temperature synthetic process.[15,16] When a mesoporous layer grown from ZnO nanorods using a chemical bath was first

[a]State Key Laboratory of Structural Chemistry, Fujian Institute of Research on the Structure of Matter, Chinese Academy of Sciences, Fuzhou, Fujian 350002, China
[b]College of Chemistry and Materials, Fujian Normal University, Fuzhou, Fujian 350007, China
[c]College of Chemistry, Fuzhou University, Fuzhou, Fujian 350002, China
[d]National Engineering Research Center of Chemical Fertilizer Catalyst, School of Chemical Engineering, Fuzhou University, Fujian, 350002, China

† Electronic supplementary information (ESI) available. See DOI: 10.1039/d0na00367k

implemented in f-PSCs, it showed a PCE of 5.0% on PET/ITO, showing a great prospect.[16] The ink-dispersed ZnO nanoparticles fabricated by the spin-coating process are widely employed as ETLs in inverted devices.[17,18] The planar solar cell configuration of PEN/ITO/ZnO/$CH_3NH_3PbI_3$/PTAA/Au delivered the highest efficiency of 15.6% at the time of publication.[19] However, the hydroxide groups in the ZnO nanoparticles are very susceptible to acid and base solutions, which is detrimental to the long-term stability of f-PSCs, leading to the degradation of the perovskite layer.[20,21] Alternatively, SnO_2 is a UV- and chemical-stable material for PSCs with a larger bandgap and higher electron mobility than TiO_2 and ZnO.[22,23] The f-PSCs based on solution-processing SnO_2 ETLs could achieve a PCE of 17.21%; however, the processing temperature of up to 180 °C is far greater than the maximum tolerable temperature (150 °C) of the flexible substrates.[24] On the other hand, though SnO_x prepared by atomic layer deposition satisfies the temperature requirements and exhibits good electron selectivity, the fabrication process inhibits its application in roll-to-roll technology and commercial appeal.[25,26] Therefore, it is necessary to search for new type ETLs with processing temperatures under 150 °C and enhance long-term stability.

Cerium oxide (CeO_x) has a wide bandgap with an effective dielectric constant, good transparency, sufficient ionic conductivity, and high-temperature stability, and has been used in various optoelectronic applications, such as light absorber in organic-dye-free solar cells, photoanode in-dye sensitized solar cells, and antireflection coating in silicon solar cells.[27,28] It is worth noting that CeO_x used recently in PSCs exhibited better photoelectric properties under 6,6-phenyl-C_{61}-butyric acid methyl ester modification or when employed as a dense diffusion barrier in the p–i–n structure.[29,30] In this study, we report CeO_x aqueous sol–gel as a precursor for ETL preparation by the UV–O_3 treatment for use in flexible n–i–p planar PSCs in the quest for a low-cost and scale-up manufacturing technology. The compact CeO_x layers treated by low-temperature annealing (LT-CeO_x), ultraviolet–ozone (UV–O_3) (UV-CeO_x), and a co-processing treatment (UV/LT-CeO_x) were characterized by studying the hydrophilicity contact angle and surface behavior. In order to verify the difference of device ETLs, photoelectric tests of the cells with, as well as without UV–O_3 treatment, were carried out. As demonstrated experimentally, the UV–O_3-treatment of the compact CeO_x layer imparted a positive effect on the cell performance, improving the efficiency from 9.08% to over 14%.

2. Experimental section

2.1 CeO_x sol–gel solution preparation

CeO_x NCs were synthesized by a modified procedure described in the literature.[31] 6.0 g of $Ce(NO_3)_3 \cdot 6H_2O$ (99%, Aldrich) was added to 70 mL distilled water with stirring till it was sufficiently dissolved. An NH_4OH (NH_3 content 28–30%, Aldrich, ACS reagent) solution was then added dropwise until a pH of 10 was reached. Then, cerium nitrate completely converted to cerium hydroxide and precipitated, which was separated by centrifugation and washed with deionized water repeatedly. Then, it was dissolved in 140 mL of a 0.1 M urea aqueous solution and adjusted to pH 2 by the addition of dilute hydrochloric acid (10%). The concentration of the obtained solution was assessed as 82 mM by calculating its xerogels at 600 °C for 2 h. The obtained CeO_x sol–gel solution was stored at room temperature to prepare ETLs.

2.2 CH_3NH_3I preparation

CH_3NH_3I was synthesized and purified using a method described in the literature.[32] 10 mL hydroiodic acid (57 wt%) was added dropwise with stirring to a 33 wt% methanol solution of methylamine (24 mL) at the temperature of 0 °C. After stirring for 2 h in an N_2 atmosphere, the obtained liquid–solid mixture was evaporated by a liquid-volatile separation process at 50 °C for 1 h to remove volatile substances. Then, the resultant crystal was permeated with three 70 mL portions of absolute diethyl ether and dried at 60 °C in a vacuum oven for 12 h to afford the desired product with high purity.

2.3 Device fabrication

ITO-coated flexible substrates (polyethylene naphthalate, PEN) were sequentially cleaned by acetone and ethanol for 15 min and then by UV–ozone (UV–O_3) treatment for another 15 min. The cleaned flexible substrates were spin-coated with the CeO_x colloid for 30 s at 2000 rpm. The UV-CeO_x ETLs were obtained after drying at 80 °C for 10 min and exposure to UV–O_3 for 15 min. The LT-CeO_x ETLs were obtained just by drying at 80 °C for 20 min. Identical processes and treating conditions were repeated for adjusting the thickness of the ETLs. After that, the ETLs were infiltrated with the perovskite precursor solution by the spin-coating process in a glovebox under a nitrogen atmosphere. The perovskite precursor solution was prepared using a stoichiometric amount of $CH_3NH_3PbI_3$ in 1.2 M DMSO with lead iodide and methyl ammonium iodide at a molar ratio of 1 : 1.[32] The spin coating procedure was firstly performed at 6000 rpm for 20 s and then for 10 s by gently dropping chlorobenzene on the spinning substrate with a micropipette. Then, the substrate was heated at 100 °C for 1 h on a hot plate in the glovebox. After they were cooled to 25 °C, the spiro-OMeTAD solution (60 μL) was spin-coated on the $CH_3NH_3PbI_3$ layer at 3000 rpm for 20 s to be used as the hole transparent layer. Spiro-OMeTAD was dissolved in chlorobenzene at 72 mg mL^{-1}, to which 28.8 μL of 4-*tert*-butyl pyridine and 14.4 μL of lithium bis(trifluoromethanesulfonyl)-imide (Li-TFSI) solution (520 mg Li-TFSI in 1 mL acetonitrile) were added. Finally, an 80 nm gold layer was deposited on the coated spiro-OMeTAD film at $\sim 10^{-6}$ bar *via* thermal evaporation.

2.4 Characterization

The XRD patterns were measured on a PANalytical X'Pert spectrometer using Co Kα radiation ($\lambda = 1.78897$ Å), and the data were converted to Cu Kα data. SEM was performed on a Hitachi S4800 instrument. TEM and SAED pattern images were recorded on a Tecnai G2 F20 (FEI) with an accelerated photo-voltage of 200 kV. The FT-IR spectra were obtained on a PerkinElmer Spectrum 2000. The survey scans were recorded using monochromatic Al

Kα irradiation, 1 eV steps and an 80 eV analyser. The transmittance spectra and UV-vis spectra were measured on a Lambda-9 (PerkinElmer) spectrometer. The steady-state photoluminescence (PL) and time-resolved photoluminescence (TRPL) decay spectra of $CH_3NH_3PbI_3$ coated on the LT-CeO_x, LT-CeO_x, and UV/LT-CeO_x ETLs were recorded using an Edinburgh FLS920 instrument with a picosecond-pulsed diode laser at 375 nm. The UPS for the LT-CeO_x, LT-CeO_x, and UV/LT-CeO_x ETLs were measured using ESCALAB 250Xi (Thermo Fisher) under a background pressure of 5.0×10^{-7} Pa.

The photovoltaic performance in terms of *J–V* characteristics was measured on a solar simulator (Sol3A Class AAA, Oriel Instruments, Stratford, CT, USA) and a Keithley 2440 source measurement unit (Keithley Instruments Inc., Cleveland, OH, USA) under 1.5 air mass (AM) and 1 sun (100 mW cm^{-2}) condition. The 1-sunlight intensity level was calibrated using a standard Si reference cell certified by the Newport Corporation. All the devices were measured in a light-tight sample holder with an active area of 0.12 cm^2 for each cell and fixed using an aperture mask. IPCE was measured using a quantum efficiency measurement system (QEX10, PV Measurements, Inc.) in the wavelength range of 300 to 850 nm. EIS was recorded using a potentiostat (IM-6, Zahner) in the frequency range of 0.1 to 100 kHz by applying the V_{oc} values derived from the *J–V* tests and under dark conditions.

3. Results and discussion

The ligand-capped CeO_x sol–gel solution prepared using a 0.1 M aqueous urea solution displayed dense uniform dispersion in deionized water without conglomeration (Fig. 1a), which is necessary for making stable, void-free and gap-filling CeO_x thin films on flexible PEN substrates. However, the cross-linking of the organic ligands in the CeO_x sol–gel solution may hinder the charge transport and deteriorate the photovoltaic performance. With this in mind, we utilized a convenient UV–O_3-processing approach to help the decomposition of organic ligands at a low temperature and reduce the spontaneous coalescence of the CeO_x nanocrystals (NCs) during preparation, thus producing high-quality ETLs. As presented in Fig. 1a, the urea-chelated CeO_x NCs self-organized into free-standing thin films by capillary-force-induced clustering of the dispersing medium during preparation.[33] Under ozone and UV-light irradiation (UV–O_3), oxygen-free radicals decomposed the urea ligands bound to the CeO_x NCs into NH_3, CO_2, and H_2O. As the organic ligands decomposed, the CeO_x NCs would congregate on plastic substrate, finally leading to the direct attachment of the CeO_x film. Without the UV–O_3 treatment, pinhole-free CeO_x thin films were successfully fabricated by the low-temperature reaction at 80 °C. In this paper, we made the first endeavor to create a dense CeO_x layer *via* ancillary ligand decomposition by applying UV–O_3 without heat treatment. The crystal structures of the CeO_x NCs before and after the UV–O_3 treatment were demonstrated by the X-ray diffraction (XRD) patterns. As shown in Fig. 1b, all the peaks in the XRD patterns of LT-CeO_x and UV-CeO_x were assignable to the cubic fluorite crystal structure (PDF no. 34-0394). We found that there was no significant difference in the microstructure between the CeO_x films obtained with and without UV–O_3 treatment. As depicted in Fig. 1c, the decomposition of the organic ligands was demonstrated by the Fourier-transform infrared (FT-IR) spectra of the CeO_x films obtained with and without UV–O_3 treatment. The bands around 3400 cm^{-1} and 1630 cm^{-1} could be ascribed to O–H stretching and bending vibrations, respectively, which are indicative of the remaining water molecules and the surface hydroxyl groups of the CeO_x thin films. The peak near 1127 cm^{-1} might be from the C–N stretching vibration of urea,[34] while the peak at 1382 cm^{-1} was due to the deformation of ammonium produced by urea decomposition.[35] Since both these peaks disappeared entirely after UV–O_3 exposure for more than 30 min, urea was entirely decomposed by free radicals under UV irradiation. The band at 1496 cm^{-1} was ascribed to the stretching vibration of the carboxylates formed from urea decomposition.[36] Lastly, the band near 480 cm^{-1} in the finger-print region corresponded to the vibrational stretching of the Ce–O bond formed under UV–O_3 treatment. Furthermore, the removal of hydrophobic molecules achieved by this simple yet efficient method was confirmed by the improved wettability of the CeO_x film in hybrid perovskite solar cells because of the hydrophilic surface of CeO_x (Fig. S1 and S2†).

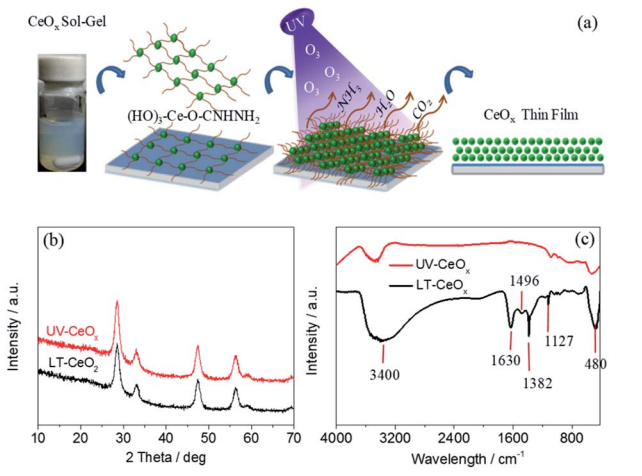

Fig. 1 (a) Schematic illustration of the UV–O_3 process for the preparation of CeO_x thin films. (b) XRD spectra and (c) FT-IR spectra of the CeO_x thin films before (LT-CeO_x) and after (UV-CeO_x) UV–O_3 treatment.

The transmission electron microscopy (TEM) images and diffraction patterns of CeO_x treated with UV–O_3 (Fig. 2) demonstrated that the CeO_x nanoparticles consisted of relatively homogeneous crystalline phases. The uniform-sized dense bodies of the CeO_x NCs were *ca.* 6 nm, which is in close agreement with the particle size values obtained from the XRD analysis, as shown in Fig. 1b. The selected area electron diffraction (SAED) patterns (Fig. 2a and b, inset) indicated that the CeO_x particles were extremely crystalline with a cubic fluorite structure, which is consistent with the XRD patterns. The TEM images of the CeO_x material without (Fig. 2a) and with (Fig. 2b) UV–O_3 treatment displayed no significant difference in morphology and crystal structure except for the larger particle size (*ca.* 10 nm) of the former.

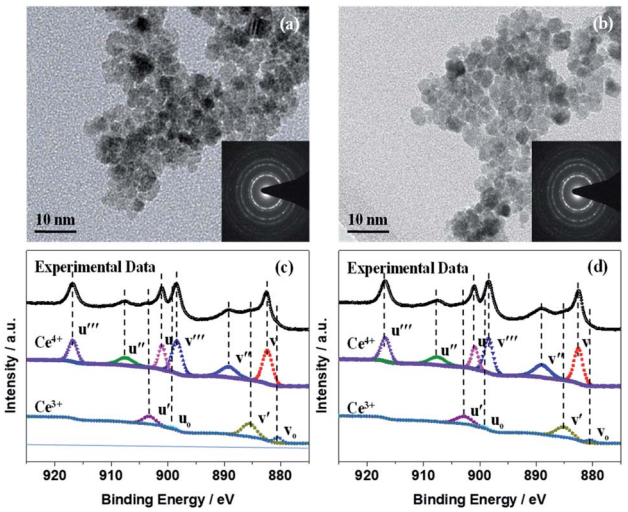

Fig. 2 (a) TEM image before UV–O_3 treatment. (b) TEM image after UV–O_3 treatment. (c) XPS spectra before UV–O_3 treatment. (d) XPS spectra after UV–O_3 treatment. Insets of (a) and (b) are the corresponding SAEDs.

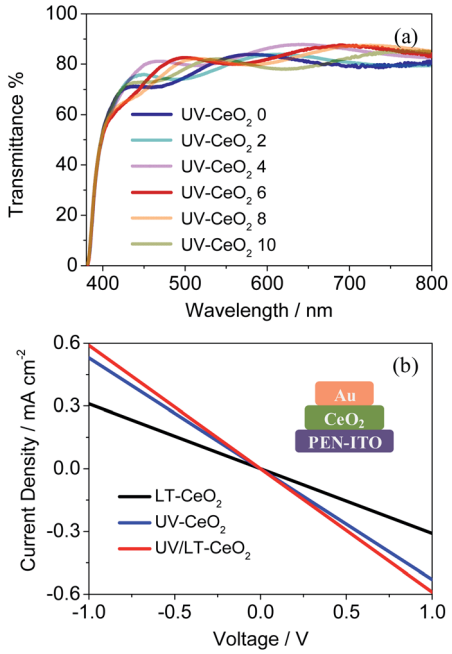

Fig. 3 (a) Transmittance spectra of the CeO_x films with different thicknesses. The number after "CeO_x" in the legend indicates the number of CeO_x ETLs spin-coated on the substrate. (b) Conductivity of the CeO_x films produced using different treatment methods.

X-ray photoelectron spectroscopy (XPS) measurements were used to confirm the composition of the CeO_x film, as depicted in Fig. 2c and d. The XPS survey scans (Fig. S4†) showed the elemental spectra of Ce, O, and C, and the adventitious C was used as the charge reference. According to an equation reported in the literature (Fig. S4†),[37,38] the concentration of Ce^{3+} was deduced from the Ce 3d spectra of the CeO_x films obtained without and with UV–O_3 treatment to be 0.27 and 0.21 (Fig. 2c and d), based on which the x values in the obtained CeO_x samples were calculated as 1.86 and 1.89, respectively. As far as variation in the elemental composition is concerned, the contents of Ce^{3+} and Ce^{4+} in the UV–O_3 treated CeO_x film were similar to those in the film prepared without the treatment.

The structural, optical and electrical properties of the CeO_x films were systematically studied to decide the aptness of CeO_x as an ETL in PSCs. In general, the UV–O_3 treatment is vital to get rid of the remaining solvents and enhance the properties of the CeO_x films.[32,39] The UV–O_3-processed CeO_x ETLs showed higher transmittance from 400 to 800 nm. As depicted in Fig. 3a, the optical transmittance of the CeO_x ETLs gradually enhanced with an increase in thickness up to 6 spin-coating cycles (71 nm). This is likely owing to the reduction in the surface roughness of the CeO_x ETLs coated on the PEN/ITO substrates relative to that of the bare PEN/ITO substrate. The top-view scanning electron microscopy (SEM) images showed a homogeneous integrated dense film on the ITO/PEN substrate spin-coated with the CeO_x sol–gel, as seen in Fig. S3.† The compact pinhole-free CeO_x films were successfully fabricated by 6 cycles of spin-coating under a UV–O_3 atmosphere, which was in favor of improving the electron transport ability and increasing the perovskite deposition quantity between particles in the mesoporous framework. The current density *versus* voltage (*J*–*V*) characteristics were analyzed to investigate the impact of the UV–O_3 treatment on electrical conductivity. The electrical conductivity of the UV/LT-CeO_x film was 1.38×10^{-4} S cm^{-1}, which was more than twice as that of the LT-CeO_x film (0.65×10^{-4} S cm^{-1}), due to the increased carrier density caused by the UV–O_3 treatment.[40,41] Noticeably, the UV-CeO_x film (1.04×10^{-4} S cm^{-1}) also exhibited higher conductivity than the LT-CeO_x film. This is because the UV–O_3 treatment hastened the disintegration of the stable surface groups and improved the links between the CeO_x nanoparticles (Fig. 3b), as well as charge transport. Meanwhile, the UV–O_3-induced epitaxial attachment of the CeO_x nanocrystals in our study was similar to that reported by Hiraide *et al.*[42]

The relationship between the thickness of the CeO_x ETL and the photovoltaic performance is illustrated in Fig. S5.† J_{sc} and V_{oc} initially enhanced as the film thickness increased, while they decreased beyond a certain film thickness. This result showed that the generation of photocurrent in CeO_x PSCs would be dominated by high-quality ETLs below *ca.* 70 nm. To understand the electron transfer pathway in CeO_x ETL, ultraviolet photoelectron spectra (UPS) and UV-vis absorbance spectra were obtained to establish the energy levels (Fig. S6†). The architecture and energy-level diagram of the CeO_x-based f-PSCs are illustrated in Fig. S7.† Therefore, planar f-PSCs based on the LT-CeO_x, UV-CeO_x and UV/LT-CeO_x ETLs were fabricated to explore their photovoltaic performance. As we know, good-quality perovskite films are key to highly-efficient stable PSCs. We prepared good quality $CH_3NH_3PbI_3$ layers on different ETLs by adopting the Lewis-base adduct approach,[43] which showed no effect on the perovskite morphology. The cross-sectional SEM image in Fig. 4a shows the device composed of typical perovskite layers: FTO/UV-CeO_x ETL (70 nm)/$CH_3NH_3PbI_3$ (480 nm)/spiro-OMeTAD (180 nm)/Au (88 nm). Fig. 4b exhibits the typical current density–voltage (*J*–*V*) curves of the cells built with

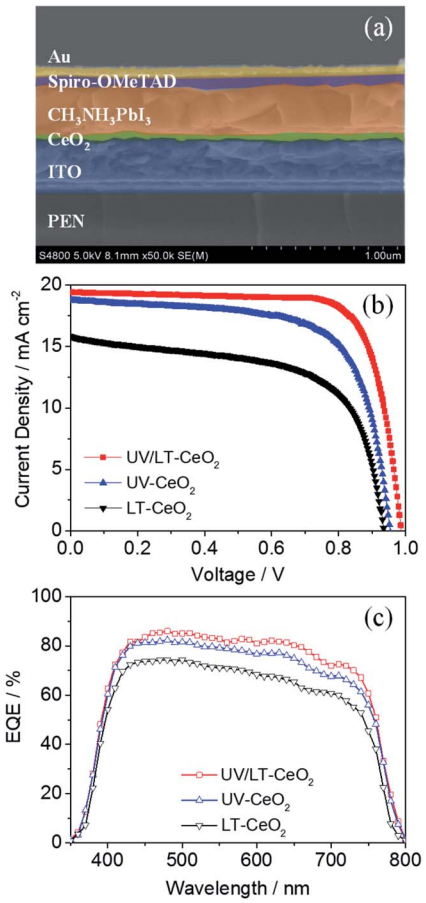

Fig. 4 (a) Cross-sectional SEM image of the f-PSC based on the UV/LT-CeO_x ETL. (b) *J*–*V* curves and (c) IPCE spectra of the high-performing f-PSCs fabricated with the LT-CeO_x, UV-CeO_x, and UV/LT-CeO_x ETLs.

the LT-CeO_x, UV-CeO_x, and UV/LT-CeO_x ETLs. The ETL dependence of various photovoltaic parameters of the solar cells is listed in Table 1. The devices based on the LT-CeO_x ETLs prepared at 80 °C exhibited a J_{sc} of 15.81 mA cm^{-2}, a V_{oc} of 0.92 V, a fill factor (FF) of 0.62, and PCE of 9.08%. In contrast, the PSCs based on the UV-CeO_x ETLs exhibited distinctly advantageous performance with a J_{sc} of 18.78 mA cm^{-2}, a V_{oc} of 0.94, an FF of 0.69, and PCE of 12.21%. When the CeO_x ETLs prepared at low temperature were irradiated by UV–O_3 treatment, the corresponding UV/LT-CeO_x-based PSCs showed remarkably higher characteristic factors with a J_{sc} of 19.42 mA cm^{-2}, a V_{oc} of 0.98 V, an FF of 0.72, and the best PCE at 14.63%. The extensive performance statistics for *ca.* 75 devices in each group can be found in Fig. S8.† The reasons for the improved performance of the UV/LT-CeO_x devices than the LT-CeO_x ones are better transparency, advantageous electrochemical properties, and the higher hole-blocking effect, which may be due to the decreased charge recombination since the UV–O_3 treatment optimizes the defects sites on the CeO_x film surface.[44,45] Fig. 4c illustrates the incident photon-to-current efficiency (IPCE) spectra of the cells. Compared with devices based on UV-CeO_x and LT-CeO_x, the broad spectral response (300–760 nm) of the UV/LT-CeO_x devices exhibited a higher IPCE value dependence, which was devoted to the exceptional optical transparency and electrical conductivity of the CeO_x ETL. The ratio of the respective integrated IPCE spectra of each batch corresponded with the ratio of the photocurrents.

Table 1 Summary of the photovoltaic performance metrics of the best and average devices based on the UV/LT-CeO_x, UV-CeO_x, LT-CeO_x ETLs under AM 1.5 illumination (100 mW cm^{-2})[a]

Sample	J_{sc}/mA cm^{-2}	V_{oc}/V	FF/%	PCE/%
LT-$CeO_{x\text{-max}}$	15.81	0.92	62.19	9.08
LT-$CeO_{x\text{-avg}}$	15.93	0.91	58.72	8.49
UV-$CeO_{x\text{-max}}$	18.78	0.94	69.31	12.21
UV-$CeO_{x\text{-avg}}$	17.75	0.93	69.89	11.56
UV/LT-$CeO_{x\text{-max}}$	19.42	0.98	76.21	14.63
UV/LT-$CeO_{x\text{-avg}}$	19.01	0.96	74.38	13.50

[a] Max and avg represent the best and the average devices, respectively.

To investigate the effect of doping UV–O_3 in detail, PL and TRPL spectroscopy were performed to probe the charge transfer process between the CeO_x ETL and the perovskite layer after UV–O_3 doping. Fig. 5a exhibits that the quenching of the intrinsic $CH_3NH_3PbI_3$ fluorescence emission by the ETLs occurred at the spectral peak (766 nm). Compared with the LT-

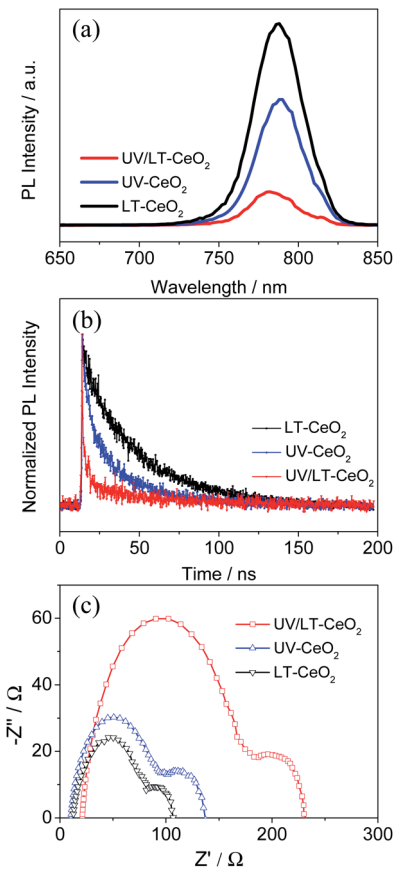

Fig. 5 (a) Normalized steady-state photoluminescence (PL) spectra, (b) normalized time-resolved photoluminescence (TRPL) spectra and (c) EIS spectra of the LT-CeO_x, UV-CeO_x, and UV/LT-CeO_x ETLs in PSCs.

CeO_x/perovskite sample, the PL intensities of UV-CeO_x/perovskite and UV/LT-CeO_x/perovskite were drastically reduced with the UV–O_3 doping process, indicating that the photocurrent density and recombination rate reduction were the most efficient in the UV–O_3-processed ETLs. A higher increase in amplitude accompanied by a slow PL quenching, produced in a progressive manner from the perovskite and its interfaces. Therefore, the UV–O_3 doping process is beneficial for speedy charge transport and enhanced charge generation and collection in the device. Fig. 5b presents the TRPL spectra and the matching PL decay times evaluated using an apparently bi-exponential decay model. The results for the LT-CeO_x/perovskite, UV-CeO_x/perovskite and UV/LT-CeO_x/perovskite samples are summarized in Table S1.† The fast decay corresponded to the quenching of carriers from the perovskite layer to the ETLs, and the slow decay was regarded as the result of irradiative decay within the perovskite film.[31,46,47] In comparison with the LT-CeO_x film, the UV-CeO_x ETL-based devices exhibited a fast decay constant decay, which dominated the charge extraction from the perovskite to the ETLs. The average lifetime at the interface between LT-CeO_x and the perovskite film was 31.20 ns, which severely decreased to 26.11 ns at the interface between UV-CeO_x and the perovskite film. In comparison with UV-CeO_x/perovskite, a faster decay component could be observed at the UV/LT-CeO_x/perovskite interface under increased amplitude (2.68 ns to 1.80 ns), which induced a low average lifetime (18.21 ns). Thus, the UPS spectra (Fig. S6b†) and PL emission spectra exhibited that charge transport and extraction were strongly enhanced by the synergistic effects of the sharp-shift in the energy level and the raised electrical conductivity, resulting in great enhancement of the photocurrent efficiency of the UV/LT-CeO_x ETL.

To further comprehend the improvement in performance upon UV–O_3 treatment, electrochemical impedance spectroscopy (EIS) measurements were carried out on different devices since it is considered as an effective method to investigate the carrier transport behavior and interfacial properties of PSCs.[48,49] The Nyquist plots displayed in Fig. 5c were obtained under dark at an applied bias voltage of 0.7 V in the frequency range from 0.1 to 100 kHz, in which two different semicircles are shown in the high- and low-frequency ranges. The Nyquist plots were fitted with an equivalent circuit containing a series resistance (R_s) in series with two RC elements. The fitted transport resistance (R_{co}) and recombination resistance (R_{rec}) were plotted in connection with UV–O_3 and thermal treatments, as illustrated in Fig. S9 and Table S2.†[50,51] When the CeO_x film was treated at 80 °C, the water molecules in the ETLs could not be effectively removed to obtain ideal transmission resistance (LT-CeO_x: R_{co} = 116.5 Ω cm^2). In contrast, upon UV–O_3 treatment, the R_{co} decreased significantly (R_{co} = 102.4 Ω cm^2 for the UV-CeO_x film and 87.8 Ω cm^2 for the UV/LT-CeO_x film), which is in accordance with the conductivity measurements (Fig. 3b). Moreover, compared with the R_{rec} of the LT-CeO_x-based interfaces (336.2 Ω cm^2), the R_{rec} of the UV-CeO_x-based interfaces had increased to 456.9 Ω cm^2, and that of the UV/LT-CeO_x-based interfaces increased to 573.6 Ω cm^2. Undoubtedly, the UV–O_3 treatment optimized the CeO_x/perovskite interface for a large part and reduced the recombination rate significantly by increasing the R_{rec}. Therefore, UV–O_3 treatment is conducive to realizing outstanding low-temperature CeO_x ETLs and achieving high-performance perovskite devices.

The low-temperature-processed ETLs subjected to the UV process are highly desirable for constructing high-performance flexible PSCs. Highly densely-packed CeO_x ETLs were effectively prepared on sputtered PEN/ITO substrates, and then typical devices with the ETL/$CH_3NH_3PbI_3$/spiro-OMeTAD/Au configuration were consecutively fabricated by conventional methods. The photograph of the flexible CeO_x-based PSC with UV–O_3 treatment is shown in Fig. 6a. The hysteresis effect under different *J–V* scans directions or rates were exhibited in PSCs, especially n–i–p planar devices.[52,53] It has been proposed in previous works that the hysteresis initiates from polarization caused by ferroelectricity, ion motion of perovskite materials, and an unbalanced flux carrier density.[54,55] As shown in Fig. 6b, we discovered that the devices based on the LT-CeO_x ETL showed large hysteresis between the forward and reverse scanning directions. Nevertheless, this hysteresis behavior was greatly lessened in the UV-CeO_x ETL devices, and the UV/LT-CeO_x ETL-based ones illustrated the smallest hysteresis among the devices. This phenomenon most likely stemmed from the reduced accumulation of interfacial charge in the UV/LT-CeO_x/

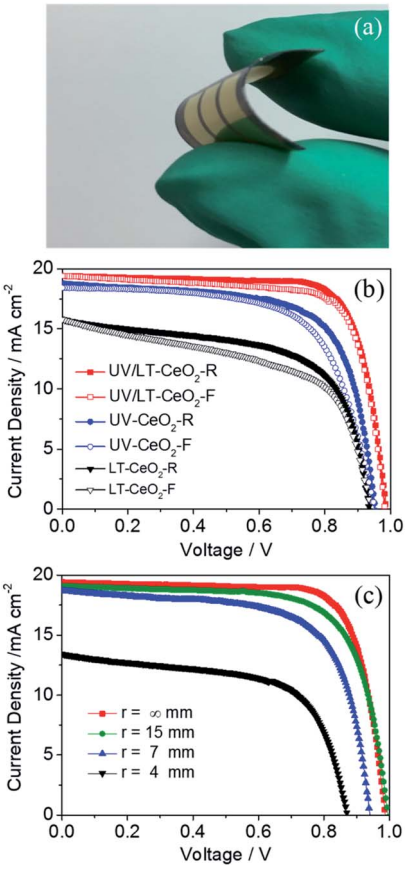

Fig. 6 (a) Photograph of the f-PSC. (b) Hysteresis behavior of the f-PSCs based on the LT-CeO_x, UV-CeO_x, and UV/LT-CeO_x ETLs, where *F* indicates the forward scan and *R* indicates the reverse scan in the *J–V* curves. (c) *J–V* curves of the f-PSCs with various radii (*r*) after recovery from 500 bending cycles.

perovskite interface. This result is consistent with the current hysteresis and photovoltaic performance. That is, the higher the charge extraction efficiency of selective contact, the lesser is the current hysteresis in the *J–V* curves, and the higher is the photovoltaic performance of the f-PSC. The stabilized photocurrents of the devices at 0.88 V bias under 1 sun illumination are tracked in Fig. S10a,† and the stabilized PCEs at the different bending radii of 15, 7 and 4 mm reached 13.96, 11.95 and 10.71% at 200 s continuous irradiation, respectively, as indicated in Fig. S10b.† To assess the stability of the devices with and without UV–O_3 treatment, the long-term stability of cells stored in the air with 10% RH at 25 °C without packing was compared. The PCEs of the devices fabricated with UV/LT, UV and LT ETLs were measured continuously for 550 h. As presented in Fig. S10c,† the half-life of the device treated with UV/LT was at least 200 h longer than the other two half-life periods. This might be due to the compact perovskite film with a low trap-state density, which could effectively resist moisture penetration. Fig. 6c shows the *J–V* curves of the f-PSC as a function of the bending curvature radius and bending cycles. The remarkable PCE of the f-PSC was 14.63%. After 500 bending cycles at $r = 15$, 7 and 4 mm, the PCE values were 13.27%, 8.53% and 4.41%, respectively. These results illustrated that the initial efficiency was reduced to *ca.* 90% at $r = 15$ mm, but was caused devastating at $r = 4$ mm. We can assume that the slight decrease in PCE at $r = 15$ mm was due to the plastic deformation of the ITO/PEN substrate. However, the brittle ITO could possibly have broken when bent at $r = 4$ mm, which is consistent with previous reports.[56,57] Meanwhile, the photovoltaic parameters (J_{sc}, V_{oc}, and FF) showed an almost similar decreased tendency with a 2% loss after 500 bending cycles. Hence, we could conclude that the structure of the cell with $r = 15$ mm possessed outstanding mechanical durability. The durability test was also performed on the three devices at $r = 15$, 7 and 4 mm, for up to 500 cycles (Fig. S10d†). When the device was deformed once, the device performance decreased linearly at the same bending radius. The cells bent at 15 mm showed excellent stability with less than 10% reduction of the PCE after repeated bending at ambient temperature.

4. Conclusions

In this work, a low-temperature process (80 °C) for preparing highly efficient f-PSCs involving UV–O_3 treatment of ligand-capped CeO_x NCs was developed. The photocatalytic decomposition of the organic ligands accompanied the spontaneous coalescence of the NCs, resulting in highly efficient ETLs, which exhibited high performance, including high film compactness, high electrical conductivity, and high transparency, as well as favorable energy levels matching with the perovskite. Using the UV–O_3 treated CeO_x ETLs prepared at a low temperature, highly efficient planar PSCs with the best PCE of 14.63% was achieved with ITO/PEN substrates. We report a facile route that is very appropriate for the construction of high-performance f-PSCs because it easily modifies the ETLs at a low-temperature. This approach will pave the way for further development of f-PSCs and is feasible for large-scale roll-to-roll processes.

Conflicts of interest

The authors declare no competing financial and nonfinancial interests.

Acknowledgements

This work was financially supported by National Natural Science Foundation of China (21603230, 21073039 and 21801242), the CAS/SAFEA International Partnership Program for Creative Research Teams, the Strategic Priority Research Program of the Chinese Academy of Sciences (XDB20000000), and Key Laboratory of Novel Thin Film Solar Cells, CAS.

References

1 J. Burschka, N. Pellet, S. J. Moon, R. H. Baker, P. Gao, M. K. Nazeeruddin and M. Grätzel, *Nature*, 2013, **499**, 316–319.
2 S. H. Turren-Cruz, A. Hagfeldt and M. Saliba, *Science*, 2018, **362**, 449–453.
3 P. B. Ru, E. B. Bi, Y. Zhang, Y. B. Wang, W. Y. Kong, Y. M. Sha, W. T. Tang, P. Zhang, Y. Z. Wu, W. Chen, X. D. Yang, H. Chen and L. Y. Han, *Adv. Energy Mater.*, 2020, **1903487**, 1–9.
4 C. C. Wu, D. Wang, Y. Q. Zhang, F. D. Gu, G. H. Liu, N. Zhu, W. Luo, D. Han, X. Guo, B. Qu, S. F. Wang, Z. Q. Bian, Z. J. Chen and L. X. Xiao, *Adv. Funct. Mater.*, 2019, **1902974**, 1–7.
5 K. Q. Huang, Y. Y. Peng, Y. X. Gao, J. Shi, H. Y. Li, X. D. Mo, H. Huang, Y. L. Gao, L. M. Ding and J. L. Yang, *Adv. Energy Mater.*, 2019, **1901419**, 1–9.
6 M. M. Lee, J. Teuscher, T. Miyasaka, T. N. Murakami and H. J. Snaith, *Science*, 2012, **338**, 643–647.
7 W. S. Yang, J. H. Noh, N. J. Jeon, Y. C. Kim, S. Ryu, J. Seo and S. I. Seok, *Science*, 2015, **348**, 1234–1237.
8 F. D. Giacomo, V. Zardetto, A. D'Epifanio, S. Pescetelli, F. Matteocci, S. Razza, A. D. Carlo, S. Licoccia, W. M. M. Kessels, M. Creatore and T. M. Brown, *Adv. Energy Mater.*, 2015, **5**, 1401808.
9 I. Jeong, H. Jung, M. Park, J. S. Park, H. J. Son, J. Joo, J. Lee and M. J. Ko, *Nano Energy*, 2016, **28**, 380–389.
10 U. Ryu, S. Jee, J. Park, K. Han, J. H. Lee, M. Park and K. M. Choi, *ACS Nano*, 2018, **12**, 4968–4975.
11 M. Lee, Y. Jo, D. S. Kim, H. Y. Jeong and Y. Jun, *J. Mater. Chem. A*, 2015, **3**, 14592–14597.
12 C. Tao, S. Neutzner, L. Colella, S. Marras, A. R. S. Kandada, M. Gandini, M. D. Bastiani, G. Pace, L. Manna, M. Caironi, C. Bertarelli and A. Petrozza, *Energy Environ. Sci.*, 2015, **8**, 2365–2370.
13 T. Leijtens, G. E. Eperon, S. Pathak, A. Abate, M. M. Lee and H. J. Snaith, *Nat. Commun.*, 2013, **4**, 3885.
14 W. Li, W. Zhang, S. V. Reenen, R. J. Sutton, J. Fan, A. A. Haghighirad, M. B. Johnston, L. Wang and H. J. Snaith, *Energy Environ. Sci.*, 2016, **9**, 490–498.
15 P. P. Boix, K. Nonomura, N. Mathews and S. G. Mhaisalkar, *Mater. Today*, 2014, **17**, 16–23.

16 D. Q. Bi, G. Boschloo, S. Schwarzmuller, L. Yang, E. M. J. Johansson and A. Hagfeldt, *Nanoscale*, 2013, **5**, 11686–11691.
17 K. Hwang, Y. S. Jung, Y. J. Heo, F. H. Scholes, S. E. Watkins, J. Subbiah, D. J. Jones, D. Y. Kim and D. Vak, *Adv. Mater.*, 2015, **27**, 1241–1247.
18 Y. Yang, J. You, Z. Hong, Q. Chen, M. Cai, T. B. Song, C. C. Chen, S. Lu, Y. Liu and H. Zhou, *ACS Nano*, 2014, **8**, 1674–1680.
19 J. H. Heo, M. H. Lee, H. J. Han, B. R. Patil, J. S. Yu and S. H. Im, *J. Mater. Chem. A*, 2016, **4**, 1572–1578.
20 J. Yang, B. D. Siempelkamp, E. Mosconi, F. D. Angelis and T. L. Kelly, *Chem. Mater.*, 2015, **27**, 4229–4236.
21 Y. Cheng, Q. D. Yang, J. Xiao, Q. Xue, H. W. Li, Z. Guan, H. L. Yip and S. W. Tsang, *ACS Appl. Mater. Interfaces*, 2015, **7**, 19986–19993.
22 Q. Wali, A. Fakharuddin, I. Ahmed, M. H. Ab Rahim, J. Ismail and R. Jose, *J. Mater. Chem. A*, 2014, **2**, 17427–17434.
23 Q. Jiang, L. Zhang, H. Wang, X. Yang, J. Meng, H. Liu, Z. Yin, J. Wu, X. Zhang and J. You, *Nat. Energy*, 2016, **2**, 16177.
24 W. Ke, G. Fang, Q. Liu, L. Xiong, P. Qin, H. Tao, J. Wang, H. Lei, B. Li, J. Wan, G. Yang and Y. Yan, *J. Am. Chem. Soc.*, 2015, **137**, 6730–6733.
25 J. P. Correa Baena, L. Steier, W. Tress, M. Saliba, S. Neutzner, T. Matsui, F. Giordano, T. J. Jacobsson, A. R. Srimath Kandada, S. M. Zakeeruddin, A. Petrozza, A. Abate, M. K. Nazeeruddin, M. Grätzel and A. Hagfeldt, *Energy Environ. Sci.*, 2015, **8**, 2928–2934.
26 C. Wang, D. Zhao, C. R. Grice, W. Liao, Y. Yu, A. Cimaroli, N. Shrestha, P. J. Roland, J. Chen, Z. Yu, P. Liu, N. Cheng, R. J. Ellingson, X. Zhao and Y. Yan, *J. Mater. Chem. A*, 2016, **4**, 12080–12087.
27 A. Corma, P. Atienzar, H. García and J. Y. C. Ching, *Nat. Mater.*, 2004, **3**, 394–397.
28 R. Jose, V. Thavasi and S. Ramakrishna, *J. Am. Ceram. Soc.*, 2009, **92**, 289–301.
29 X. Wang, L. L. Deng, L. Y. Wang, S. M. Dai, Z. Xing, X. X. Zhan, X. Z. Lu, S. Y. Xie, R. B. Huang and L. S. Zheng, *J. Mater. Chem. A*, 2017, **5**, 1706–1712.
30 T. Hu, S. Q. Xiao, H. J. Yang, L. Chen and Y. W. Chen, *Chem. Commun.*, 2018, **54**, 471–474.
31 P. Periyat, F. Laffir, S. A. M. Tofaila and E. Magner, *RSC Adv.*, 2011, **1**, 1794–1798.
32 A. Y. Pang, D. L. Shen, M. D. Wei and Z. N. Chen, *ChemSusChem*, 2018, **11**, 424–431.
33 S. C. Pillai, P. Periyat, R. G. Kutty, D. E. McCormack, M. K. Seery, H. Hayden, J. Colreavy, D. Corr and S. J. Hinder, *J. Phys. Chem. C*, 2007, **111**, 1605–1611.
34 L. Ren, X. Huang, F. Sun and X. He, *Mater. Lett.*, 2007, **61**, 427–431.
35 H. Gu and M. D. Soucek, *Chem. Mater.*, 2007, **19**, 1103–1110.
36 Z. A. Tan, L. Li, C. Li, L. Yan, F. Wang, J. Xu, L. Yu, B. Song, J. Hou and Y. Li, *Adv. Mater. Interfaces*, 2014, **1**, 1400197.
37 S. Watanabe, X. Ma and C. Song, *J. Phys. Chem. C*, 2009, **113**, 14249–14257.
38 K. H. Jung, J. Y. Seo, S. Lee, H. Shin and N. G. Park, *J. Mater. Chem. A*, 2017, **5**, 24790–24803.
39 W. Ke, D. Zhao, A. J. Cimaroli, C. R. Grice, P. Qin, Q. Liu, L. Xiong, Y. Yan and G. Fang, *J. Mater. Chem. A*, 2015, **3**, 24163–24168.
40 T. Nikolay, L. Larina, O. Shevaleevskiy and B. T. Ahn, *Energy Environ. Sci.*, 2011, **4**, 1480–1486.
41 W. Chen, Y. Wu, Y. Yue, J. Liu, W. Zhang, X. Yang, H. Chen, E. Bi, I. Ashraful, M. Grätzel and L. Han, *Science*, 2015, **350**, 944–948.
42 T. Hiraide, H. Kageyama, Y. Nakagawa, Y. Oaki and H. Imai, *Chem. Commun.*, 2016, **52**, 7545–7548.
43 N. Ahn, D. Y. Son, I. H. Jang, S. M. Kang, M. Choi and N. G. Park, *J. Am. Chem. Soc.*, 2015, **137**, 8696–8799.
44 D. H. Kim, G. S. Han, W. M. Seong, J. W. Lee, B. J. Kim, N. G. Park, K. S. Hong, S. Lee and H. S. Jung, *ChemSusChem*, 2015, **8**, 2392–2398.
45 X. Lü, X. Mou, J. Wu, D. Zhang, L. Zhang, F. Huang, F. Xu and S. Huang, *Adv. Funct. Mater.*, 2010, **20**, 509–515.
46 G. Niu, W. Li, F. Meng, L. Wang, H. Dong and Y. Qiu, *J. Mater. Chem. A*, 2014, **2**, 705–710.
47 B. Duan, Y. K. Ren, Y. F. Xu, W. Y. Chen, Q. Ye, Y. Huang, J. Zhu and S. Y. Dai, *Inorg. Chem. Front.*, 2017, **4**, 473–480.
48 T. Bu, L. Wu, X. Liu, X. Yang, P. Zhou, X. Yu, T. Qin, J. Shi, S. Wang, S. Li, Z. Ku, Y. Peng, F. Huang, Q. Meng, Y. B. Cheng and J. Zhong, *Adv. Energy Mater.*, 2017, **7**, 1700576.
49 I. Zarazua, G. Han, P. P. Boix, S. Mhaisalkar, F. FabregatSantiago, I. Mora-Sero, J. Bisquert and G. Garcia-Belmonte, *J. Phys. Chem. Lett.*, 2016, **7**, 5105–5113.
50 J. Dagar, S. Castro-Hermosa, M. Gasbarri, A. L. Palma, L. Cina, F. Matteocci, E. Calabro, A. D. Carlo and T. M. Brown, *Nano Res.*, 2018, **11**, 2669–2681.
51 T. Bu, S. W. Shi, J. Li, Y. F. Liu, J. L. Shi, L. Chen, X. P. Liu, J. H. Qiu, Z. L. Ku, Y. Peng, J. Zhong, Y. B. Cheng and F. Z. Huang, *ACS Appl. Mater. Interfaces*, 2018, **10**, 14922–14929.
52 H. J. Snaith, A. Abate, J. M. Ball, G. E. Eperon, T. Leijtens, N. K. Noel, S. D. Stranks, J. T. W. Wang, K. Wojciechowski and W. Zhang, *J. Phys. Chem. Lett.*, 2014, **5**, 1511–1515.
53 J. H. Heo, H. J. Han, D. Kim, T. K. Ahn and S. H. Im, *Energy Environ. Sci.*, 2015, **8**, 1602–1608.
54 Y. Shao, Z. Xiao, C. Bi, Y. Yuan and J. Huang, *Nat. Commun.*, 2014, **5**, 5784.
55 C. Li, S. Tscheuschner, F. Paulus, P. E. Hopkinson, J. Kießling, A. Köhler, Y. Vaynzof and S. Huettner, *Adv. Mater.*, 2016, **28**, 2446–2454.
56 B. J. Kim, D. H. Kim, Y. Y. Lee, H. W. Shin, G. S. Han, J. S. Hong, K. Mahmood, T. K. Ahn, Y. C. Joo, K. S. Hong, N. G. Park, S. Lee and H. S. Jung, *Energy Environ. Sci.*, 2015, **8**, 916–921.
57 J. W. Jo, M. S. Seo, M. Park, J. Y. Kim, J. S. Park, I. K. Han, H. Ahn, J. W. Jung, B. H. Sohn, M. J. Ko and H. J. Son, *Adv. Funct. Mater.*, 2016, **26**, 4464–4471.